

Amplitude Mode in Quantum Magnets via Dimensional Crossover

Chengkang Zhou,¹ Zheng Yan,^{1,2} Han-Qing Wu,³ Kai Sun,^{4,*} Oleg A. Starykh,^{5,†} and Zi Yang Meng^{1,‡}

¹*Department of Physics and HKU-UCAS Joint Institute of Theoretical and Computational Physics, The University of Hong Kong, Pokfulam Road, Hong Kong SAR, China*

²*State Key Laboratory of Surface Physics and Department of Physics, Fudan University, Shanghai 200438, China*

³*School of Physics, Sun Yat-Sen University, Guangzhou, 510275, China*

⁴*Department of Physics, University of Michigan, Ann Arbor, Michigan 48109, USA*

⁵*Department of Physics and Astronomy, University of Utah, Salt Lake City, Utah 84112, USA*

(Dated: May 20, 2021)

We investigate the amplitude (Higgs) mode associated with longitudinal fluctuations of the order parameter at the continuous spontaneous symmetry breaking phase transition. In quantum magnets, due to the fast decay of the amplitude mode into low-energy Goldstone excitations, direct observation of this mode represents a challenging task. By focusing on a quasi-one-dimensional geometry, we circumvent the difficulty and investigate the amplitude mode in a system of weakly coupled spin chains with the help of quantum Monte Carlo simulations, stochastic analytic continuation, and a chain-mean field approach combined with a mapping to the field-theoretic sine-Gordon model. The amplitude mode is observed to emerge in the longitudinal spin susceptibility in the presence of a weak symmetry-breaking staggered field. A conventional measure of the amplitude mode in higher dimensions, the singlet bond mode, is found to appear at a lower than the amplitude mode frequency. We identify these two excitations with the second (first) breather of the sine-Gordon theory, correspondingly. In contrast to higher-dimensional systems, the amplitude and bond order fluctuations are found to carry significant spectral weight in the quasi-1D limit.

Introduction.— The phenomenon of spontaneous symmetry breaking (SSB) represents one of the key notions in modern physics. For a continuous global symmetry, SSB is expected to generate two types of collective excitations – Goldstone modes, describing transverse or phase fluctuations of the order parameter, and Higgs modes, which describe its longitudinal or amplitude fluctuations. In contrast to the gapless Goldstone excitation, which is commonly observed in a variety of condensed matter systems (e.g., magnons in magnetically ordered materials), the observation of the amplitude (longitudinal) mode is more challenging. It is complicated by its intrinsically finite lifetime – an amplitude-mode excitation is allowed to decay into a pair of Goldstone excitations which leads to a strong damping of this excitation. By now several successful experimental sightings of the amplitude mode have been reported in the dimerized [1] and quasi-one-dimensional (1D) quantum magnets KCuF_3 [2, 3], $\text{BaCu}_2\text{Si}_2\text{O}_7$ [4], Ising-like spin chains $\text{SrCo}_2\text{V}_2\text{O}$ and $\text{Yb}_2\text{Pt}_2\text{Pb}$ [5, 6] as well as in superconducting settings [7, 8].

The amplitude mode is a well-defined excitation when its lifetime is long, which requires suppression of the decays into Goldstone modes, the spin waves. Theoretically, such suppression requires weakening of the long range magnetic order, the magnitude of which determines the spectral weight of the spin waves. Two ways to achieve this have been proposed, through (a) quantum critical points (QCPs) [9–12] and (b) dimensional crossover towards one dimension (1D) [13–16]. The first strategy was recently verified via quantum Monte Carlo model simulations in dimerized antiferromagnet [17–19] and superconductor-insulator transition [20].

In this Letter, we explore the second, quasi-1D approach. It has long been proposed that a stable longitudinal mode shall arise in weakly coupled spin chains [14–16]. It should be noted that this 1D critical point is strongly different from

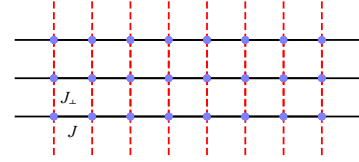


FIG. 1. Coupled antiferromagnetic Heisenberg spin chains with nearest-neighbor spin exchange J (black solid line) and J_\perp (red dashed line).

the $O(3)$ QCP one due to the extreme spatial anisotropy of spin correlations. At the critical point, which corresponds to the limit of decoupled spin chains, excitations propagate only along chains. This feature, combined with unique properties of the spin-1/2 Heisenberg chain, imbues the ordered phase of weakly coupled spin-1/2 chains with the spinon confinement physics which is absent in the spatially isotropic magnetically ordered phase with spontaneously broken $O(3)$ symmetry.

To study the excitation spectrum of the quasi-1D spin system, we utilize quantum Monte Carlo (QMC) simulations and stochastic analytic continuation (SAC) [21–23] to compute the spectral information of weakly coupled Heisenberg spin-1/2 chains. The predicted amplitude modes are directly observed in the numerics as the interchain interaction is reduced towards zero, and the dispersions of all low-energy modes agree nicely with analytic predictions. More importantly, we find that the amplitude mode in quasi-1D systems exhibits two novel features. First, in contrast with higher-dimensional magnets, the amplitude mode in quasi-1D systems is characterized by a spectral weight significantly stronger than the continuum, making it highly visible and easy to detect. Second, we find that a quasi-1D spin-1/2 magnet contains *three*, instead of two, low-energy modes. In addition to the phase

and amplitude modes, visible in the dynamic spin correlation functions, an additional scalar mode emerges in the dynamic *bond correlation* function. Similar to the amplitude mode, this scalar mode is singletlike but exhibits different frequency and momentum dependence.

In higher dimensions, it has been known that the scalar susceptibility serves as a great tool for probing fluctuations in the singlet channel [10] and has been widely used in numerical studies of dimerized antiferromagnets [17–19]. Inside the ordered SSB phase scalar fluctuations overlap with the amplitude ones but with much suppressed damping, and the scalar susceptibility exhibits a sharp peak at the amplitude mode frequency [11]. The quasi-1D limit is different. We show that in contrast to the amplitude mode which corresponds to the “second breather” in the effective sine-Gordon description of the ordered quasi-1D magnet, the scalar mode is represented by the “first breather”, an excitation with smaller frequency which is probed via the dynamic bond-bond correlation function.

The model and the QMC method.— The geometry of the problem is shown in Fig. 1. The Hamiltonian reads

$$H = J \sum_{\langle i,j \rangle_x} \mathbf{S}_i \cdot \mathbf{S}_j + J_\perp \sum_{\langle i,j \rangle_y} \mathbf{S}_i \cdot \mathbf{S}_j - h \sum_i (-1)^i S_i^z, \quad (1)$$

where $\mathbf{S}_i = (S_i^x, S_i^y, S_i^z)$ denotes the spin-1/2 operator on site i and J (J_\perp) is the nearest-neighbor Heisenberg exchange along the x (y) direction. We set $J = 1$ and introduce ratio $g = J_\perp/J$ to control the crossover from decoupled 1D chains, $g = 0$, to the isotropic 2D square lattice, $g = 1$. The last term represents the staggered pinning field h , which explicitly breaks the spin-rotational symmetry.

In our QMC simulations the following three correlation functions are measured: the transverse spin correlation function $G_{S^x}(\mathbf{q}, \tau) = \frac{1}{L^2} \sum_{i,j} e^{-i\mathbf{q} \cdot (\mathbf{r}_i - \mathbf{r}_j)} \langle S_i^x(\tau) S_j^x(0) \rangle$, the similarly defined longitudinal S^z correlation function $G_{S^z}(\mathbf{q}, \tau)$, and the bond correlation $G_B(\mathbf{q}, \tau) = \frac{1}{L^2} \sum_{i,j} e^{-i\mathbf{q} \cdot (\mathbf{r}_i - \mathbf{r}_j)} \langle B_j(\tau) B_i(0) \rangle$. Here $B_i = \mathbf{S}_i \cdot \mathbf{S}_{i+\hat{x}}$ is a spin singlet bond operator (dimerization order parameter) defined on a nearest-neighbor bond of the spin chain, L is the linear system size and $\tau \in [0, \beta]$ is the imaginary time. In the ordered the SSB ground state with finite $\langle S^z \rangle \neq 0$ phase fluctuations (spin waves) are probed by G_{S^x} , G_{S^z} measures the amplitude fluctuations, and the scalar correlation function G_B probes correlations between bonds (energy density) [17–19].

It is important to notice that SSB ground state is not possible in the QMC simulation on a finite $L \times L$ system and at finite inverse temperature β . Therefore, in the QMC with $h = 0$, there is no distinction between the phase and amplitude correlation functions, $G_{S^x}(\mathbf{q}, \tau) = G_{S^z}(\mathbf{q}, \tau)$. Finite $h \neq 0$ breaks spin-rotational symmetry and allows one to probe the amplitude mode by measuring G_{S^z} . It also induces the h -dependent gap in the phase mode in G_{S^x} [24–26].

In order to access real-time quantum dynamics and obtain the real-frequency spectral function $A(\mathbf{q}, \omega)$ from the imaginary-time correlation $G(\mathbf{q}, \tau)$,

$G(\mathbf{q}, \tau) = \frac{1}{\pi} \int_0^\infty d\omega A(\mathbf{q}, \omega) (e^{-\tau\omega} + e^{-(\beta-\tau)\omega})$, we employ the stochastic analytic continuation (SAC). This technique, details of which are described in Refs. [27–30] and the Supplemental Material (SM) [31], has been successfully applied to a broad range of quantum magnets [32–41].

Analytical theory.— At small $g = J_\perp/J \ll 1$, a variety of exact (Bethe ansatz) and nonperturbative approaches (bosonization and renormalization group) are available. In the $g = 0$ limit elementary excitations of the spin chain are right- and left-moving spinons, neutral spin-1/2 fermions $\psi_{R/L,s}$, which encode an extended $SU(2)_R \times SU(2)_L$ symmetry of chiral rotations at low energies. The staggered part of the lattice spin operator is expressed via spinons as $S_i^a \sim (-1)^i \psi_{R,s}^\dagger \sigma_{ss'}^a \psi_{L,s'} + \text{H.c.}$, where σ^a is the Pauli matrix. The singlet bond operator is staggered as well $B_i \sim (-1)^i \psi_{R,s}^\dagger \psi_{L,s} + \text{H.c.}$. These expressions define physical response functions G_{S^a} and G_B of the chain. When continued to the real frequency, the response is given by the triplet and singlet spinon continua, correspondingly.

Interchain interaction, $g \neq 0$, causes *confinement of spinons*, binding them in triplet and singlet pairs. This is easiest seen with the help of the chain mean-field theory [15, 16, 42, 43] which maps the problem to the 1D sine-Gordon model by approximating the J_\perp term in Eq. (1) by the interchain staggered field $2J_\perp m_0 \sum_i (-1)^i S_i^z$ with the self-consistently determined staggered magnetic order $m_0 = (-1)^i \langle S_i^z \rangle$ along the z axis [31]. This mean field breaks spin rotational symmetry of the problem (with $h = 0$). The excitation spectrum of the sine-Gordon model consists of solitons and antisolitons of mass Δ_0 , which describe transverse spin excitations, and their bound states, breathers. The amplitude mode, which within the low-energy mapping to the sine-Gordon model is represented by $S^z \sim \cos(\Phi/2)$, is described by the *second* breather, of mass $\sqrt{3}\Delta_0$. The singlet mode, which is represented as $B \sim \sin(\Phi/2)$, is instead described by the *first* breather, of mass Δ_0 , see Ref.[31] and Refs. [16, 43]. This brief description shows that in the system of weakly coupled spin-1/2 chains the amplitude, S^z , and the scalar, B , modes are distinct and *independent* excitations.

Detailed calculation of spin and bond susceptibilities are presented in the SM [31]. The dispersions of the phase (S^x and S^y), amplitude (S^z) and bond (B) modes near $k_x = \pi$ are

$$\omega_{S^x} = \omega_{S^y} = \Delta_0 \sqrt{1 + b_h + \cos k_y + \frac{v^2(k_x - \pi)^2}{\Delta_0^2}} \quad (2)$$

$$\omega_{S^z} = \Delta_0 \sqrt{3(1 + b_h) + \frac{Z_2}{Z_1} \cos k_y + \frac{v^2(k_x - \pi)^2}{\Delta_0^2}} \quad (3)$$

$$\omega_B = \Delta_0 \sqrt{1 + b_h + \frac{v^2(k_x - \pi)^2}{\Delta_0^2}} \quad (4)$$

Here k_x (k_y) is the momentum along the chain (transverse to the chain) and b_h is a dimensionless parameter describing the effect of the external staggered field h , Eq. (S25). At $h = 0$, b_h vanishes and our equations for ω_{S^x} and ω_{S^z} recover the

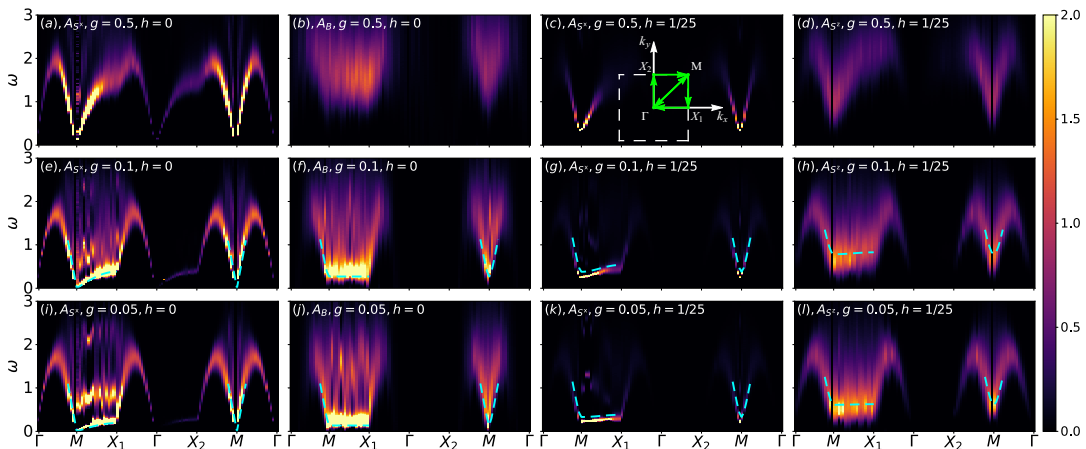


FIG. 2. Spectral functions obtained from QMC-SAC. (a), (e), (i) and (b), (f), (j) show the spectra function of spin and bond operators respectively, $A_{S^x}(\mathbf{q}, \omega)$ and $A_B(\mathbf{q}, \omega)$, without the field, $h = 0$, at different values of $g = J/J_\perp$, with the system size is $L = 36$ and inverse temperature $\beta = 4L$. The dashed cyan curves in (e), (i) and (f), (j) are analytical dispersions in Eqs. (2) and (4) with $b_h = 0$. (c), (g), (k) and (d), (h), (l) show the phase mode spectra $A_{S^x}(\mathbf{q}, \omega)$ and amplitude mode spectra $A_{S^z}(\mathbf{q}, \omega)$ measured in the presence of a weak staggered field $h = 1/25$, with system size $L = 36$ and inverse temperature $\beta = 4L$. The dashed cyan curves in (g), (k) and (h), (l) are analytical dispersions in Eqs. (2) and (3) with finite b_h .

corresponding formulae in Ref. [43]. The velocity v is $\pi J/2$ and the ratio $Z_2/Z_1 \approx 0.491309$.

Note that in addition to having a different mass, the dispersion of the bond mode is different from the amplitude one as well. It propagates along the chain with the same velocity v as spin fluctuations but is essentially dispersionless in the transverse k_y direction, see Ref.[31].

Numerical results.— In Fig. 2, we present numerical results of spectral functions for spin-spin and bond-bond correlations, with and without the pinning field h and compare them with the dispersions (cyan lines) obtained from analytic theory Eqs.(2)-(4). From the top to bottom row, the values of g are 0.5, 0.1 and 0.05, reflecting the dimensional crossover from 2D to quasi-1D. The system has periodic boundary condition $L \times L$ with $L = 36$. The QMC calculations are carried out at inverse temperature $\beta = 4L$. The spectra are plotted along the high-symmetry path indicated in the BZ in panel Fig. 2(c). The first (last) two columns of Fig. 2 are measured in the absence (presence) of the staggered field h .

Key differences between the 2D [$g = 0.5$, Figs.2(a)-2(d)] and quasi-1D regimes [$g = 0.1$ for Figs.2(e)-2(h) and $g = 0.05$ for Figs.2(j)-2(l)] are easily seen. For $g = 0.5$ the phase mode is clearly visible in panels (a) and (c) while the amplitude and scalar fluctuations (d) and (b) exhibit only an overdamped multimagnon continuum without any sharp modes, as expected [13, 14]. As the system moves towards 1D ($g = 0.1$ and 0.05), the single magnon mode remains sharp and becomes more 1D-like (i.e. less dispersive along the interchain $M - X_1$ direction). At the same time, the spectral weight in the bond [Figs.2(f) and 2(j)] and amplitude [Figs.2(h) and 2(i)] sectors shifts down in energy, resulting in the emergence of the two low energy peaks in corresponding spectral densities.

Let us investigate these differences closer. The first column

in Fig. 2 shows A_{S^x} at $h = 0$. Note that simulations in finite size and temperature system are necessarily done in the symmetric phase with three components of spin susceptibility degenerate $A_{S^x} = A_{S^y} = A_{S^z}$. The minimal spin excitation energy, measured at the M point (π, π) , is small but finite. At $g = 0.05$ it is about 0.004. The dispersion of the lowest energy branch is well described by the pole of the RPA susceptibility Eq. (S35). Notice that in this magnetically disordered phase the gap is $\Delta^2 - 2Z_1 J_\perp > 0$, as discussed above. It vanishes only in the thermodynamic limit $L = \infty$ when the SSB takes place and the spin rotational symmetry gets broken, resulting in different dispersion relations for transverse, Eq. (2), and longitudinal, Eq. (3), modes (with $b_h = 0$).

We also observe noticeable spectral intensity at higher energy, $\omega \approx 0.6 - 0.7$, in Figs.2 (e) and 2(i). We assign this to the second breather of the sine-Gordon+RPA theory, Eq. (S36), with the mass $\sqrt{3}\Delta$ [31]. Naturally, this feature is absent in the 2D limit, Fig. 2(a), where our quasi-1D arguments do not apply. This interpretation is further supported by the data for bond spectral function A_B , presented in the second column of Fig. 2. Here, one observes pronounced difference between the 2D, $g = 0.5$, and 1D limits, $g = 0.05$ and 0.1: the broad and overdamped multiparticle continuum evolves into a very structured one with a sharp particlelike peak at the lowest energy for small- g cases, in Figs.2(f) and 2(j). This is the first breather of the sine-Gordon model, describing the scalar bond (staggered dimerization) mode, with mass Δ , of weakly coupled spin chains, as described below Eq. (4). As explained in the SM [31], its dispersion along k_y is negligible while that along k_x matches Eq. (4) (with $b_h = 0$) very well.

Taken together, our data lend strong support to the description of the spin system in terms of *confined* spinon pairs. The spin susceptibility is described by the triplet of bound spinons

and its internal excited state (the second breather) while the scalar susceptibility is represented by bound singlet pairs of spinons.

To differentiate between the transverse and longitudinal fluctuations we next turn on the staggered field $h \neq 0$ along the z axis. The corresponding QMC data are represented by the last two columns of Fig. 2. Now $A_{S^x} = A_{S^y}$ measures the phase fluctuations of the order parameter (the third column), which are gapped stronger by the finite h , while A_{S^z} gives the amplitude fluctuations (the last column).

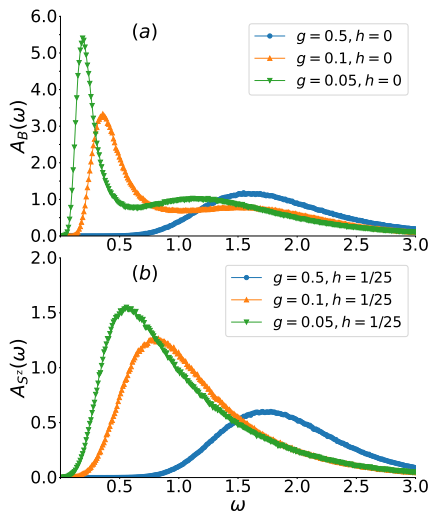


FIG. 3. Frequency dependence of the spectral functions at $\mathbf{k} = (\pi, \pi/2)$ for (a) the bond-bond correlation at $h = 0$ and (b) the amplitude mode at $h = 1/25$.

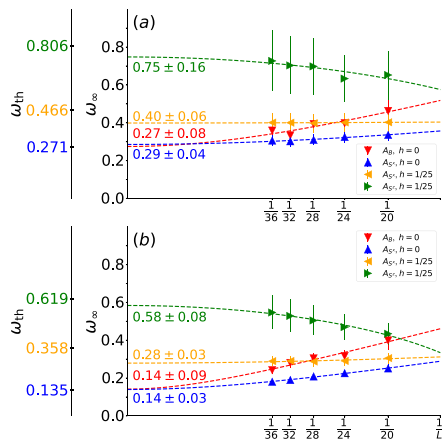


FIG. 4. Finite-size analysis for (a) $g = 0.1$ and (b) $g = 0.05$ at the momentum point $\mathbf{k} = (\pi, \pi/2)$. The vertical ω_∞ axis shows extrapolation of the numerical data to the $L = \infty$ limit. Values on the left vertical ω_{th} axis mark analytical predictions for the peak frequencies of different modes. See main text for details.

To illustrate the emergence of the amplitude and scalar modes we plot in Fig. 3 the frequency dependence of these two spectra at different values of g at the wave vector $\mathbf{k} = (\pi, \pi/2)$.

In 2D ($g = 0.5$), both spectra exhibit a continuum background from multimagnon excitations. As g gets smaller, a peak emerges in the spectral function and becomes sharper as g becomes smaller. It is seen that for the same value of g the peak in A_B is more narrow and occurs at a lower frequency than that in A_{S^z} . The larger linewidth of the amplitude mode is due to the stronger damping it experiences due to decays into the low energy phase fluctuations, in comparison with the bond correlation function [10], while the peak's maxima difference is a unique property of quasi-1D system as Eqs. (3) and (4) show.

In Fig. 4, we present the finite-size analysis and extrapolate the peak frequency of each mode to the thermodynamic limit. Here, we focus on the momentum point $\mathbf{k} = (\pi, \pi/2)$, at which the interchain dispersion vanishes within the RPA approximation, and the frequency of a mode is obtained by fitting the correlation function to an exponential function of the imaginary time $\propto e^{-\omega\tau}$ (several representative cases of such fitting are presented in SM [31]). Given the square-root form of dispersions (2), (3) and (4), we take the following functional form for the extrapolation to infinite size $\omega_L = \sqrt{\omega_\infty^2 + L_0^2/L^2}$, where ω_∞ and L_0 are fitting parameters. The results for so obtained ω_∞ are presented to the right of the ω_∞ axis in Fig. 4. As discussed above, without the staggered field the lowest energy peak in $A_{S^x}(h = 0)$ describes coherent threefold degenerate mode ω_{S^x} . At finite $h = 1/25$, the degeneracy is removed and ω_{S^x} and ω_{S^z} scale to different limits. Within the sine-Gordon description $\omega_{S^z}/\omega_{S^x} = \sqrt{3}$, see Eqs. (2) and (3). Figure 4 shows that this ratio extrapolates to 1.8 for $g = 0.1$ and to 2.0 for $g = 0.05$ at $L = \infty$. The ω_{th} axis in Fig. 4 shows analytical predictions for ω_{S^x} , ω_{S^z} , which are calculated as functions of g and h , without any adjustable parameters, in the SM [31]. This parameter-free comparison is seen to work reasonably well. In addition, in agreement with analytical predictions, Fig. 4 shows that for $h = 0$, ω_{S^x} and ω_B extrapolate to the same limit, just as Eqs. (2) and (4) with $b_h = 0$ require.

Summary.— Our main finding is that in quasi-1D limit collective amplitude and scalar modes appear in dynamic spin and bond susceptibilities, as is seen in Figs. 2 and 3, while contributions from multi-particle continua are much weaker and subleading. This needs to be contrasted with the vicinity of the O(3) QCP in higher dimensions [11, 18, 19], where the situation is the opposite. This makes spin-1/2 quasi-1D magnets an attractive candidate systems for studying collective quantum dynamics theoretically and experimentally.

O.A.S. thanks Sasha Chernyshev for insightful discussions. C.K.Z., Z.Y. and Z.Y.M. acknowledge the support from the RGC of Hong Kong SAR China (Grants No. 17303019, No.17301420, and No.AoE/P-701/20), and MOST through the National Key Research and Development Program (2016YFA0300502). O.A.S. was supported by the NSF CMMT program under Grant No.DMR-1928919. H.Q.W. is thankful for supports from NSFC-11804401 and the Fundamental Research Funds for the Central Universities (19lgpy266). We thank the Computational Initiative at the

Faculty of Science and the Information Technology Services at the University of Hong Kong and the National Supercomputer Centers in Guangzhou and Beijing PARATERA Tech CO.,Ltd. for their technical support and providing generous HPC resources that have contributed to the research results reported within this paper. This research was initiated at the Aspen Center for Physics, supported by NSF PHY-1066293.

* sunkai@umich.edu

† starykh@physics.utah.edu

‡ zymeng@hku.hk

- [1] P. Merchant, B. Normand, K. W. Krämer, M. Boehm, D. F. McMorrow, and C. Rüegg, *Nature Physics* **10**, 373 (2014).
- [2] B. Lake, D. A. Tennant, and S. E. Nagler, *Phys. Rev. Lett.* **85**, 832 (2000).
- [3] B. Lake, D. A. Tennant, and S. E. Nagler, *Phys. Rev. B* **71**, 134412 (2005).
- [4] A. Zheludev, M. Kenzelmann, S. Raymond, T. Masuda, K. Uchinokura, and S.-H. Lee, *Phys. Rev. B* **65**, 014402 (2001).
- [5] A. K. Bera, B. Lake, F. H. L. Essler, L. Vanderstraeten, C. Hubig, U. Schollwöck, A. T. M. N. Islam, A. Schneidewind, and D. L. Quintero-Castro, *Phys. Rev. B* **96**, 054423 (2017).
- [6] W. J. Gannon, I. A. Zaliznyak, L. S. Wu, A. E. Feiguin, A. M. Tsvelik, F. Demmel, Y. Qiu, J. R. D. Copley, M. S. Kim, and M. C. Aronson, *Nat. Commun.* **10**, 1123 (2019).
- [7] D. Sherman, U. S. Pracht, B. Gorshunov, S. Poran, J. Jesudasan, M. Chand, P. Raychaudhuri, M. Swanson, N. Trivedi, A. Auerbach, M. Scheffler, A. Frydman, and M. Dressel, *Nature Physics* **11**, 188 (2015).
- [8] R. Shimano and N. Tsuji, *Annu. Rev. Condens. Matter Phys.* **11**, 103 (2020).
- [9] S. Sachdev, *Phys. Rev. B* **59**, 14054 (1999).
- [10] D. Podolsky, A. Auerbach, and D. P. Arovas, *Phys. Rev. B* **84**, 174522 (2011).
- [11] S. Gazit, D. Podolsky, and A. Auerbach, *Phys. Rev. Lett.* **110**, 140401 (2013).
- [12] H. D. Scammell and O. P. Sushkov, arXiv e-prints , arXiv:1705.09007 (2017), arXiv:1705.09007 [cond-mat.str-el].
- [13] C. M. Canali and S. M. Girvin, *Phys. Rev. B* **45**, 7127 (1992).
- [14] I. Affleck and G. F. Wellman, *Phys. Rev. B* **46**, 8934 (1992).
- [15] H. J. Schulz, *Phys. Rev. Lett.* **77**, 2790 (1996).
- [16] F. H. L. Essler, A. M. Tsvelik, and G. Delfino, *Phys. Rev. B* **56**, 11001 (1997).
- [17] M. Lohöfer, T. Coletta, D. G. Joshi, F. F. Assaad, M. Vojta, S. Wessel, and F. Mila, *Phys. Rev. B* **92**, 245137 (2015).
- [18] Y. Q. Qin, B. Normand, A. W. Sandvik, and Z. Y. Meng, *Phys. Rev. Lett.* **118**, 147207 (2017).
- [19] M. Lohöfer and S. Wessel, *Phys. Rev. Lett.* **118**, 147206 (2017).
- [20] M. Swanson, Y. L. Loh, M. Randeria, and N. Trivedi, *Phys. Rev. X* **4**, 021007 (2014).
- [21] A. W. Sandvik, in *AIP Conference Proceedings*, Vol. 1297 (AIP, 2010) pp. 135–338.
- [22] O. F. Syljuåsen and A. W. Sandvik, *Phys. Rev. E* **66**, 046701 (2002).
- [23] F. Alet, S. Wessel, and M. Troyer, *Phys. Rev. E* **71**, 036706 (2005).
- [24] I. Affleck and M. Oshikawa, *Phys. Rev. B* **60**, 1038 (1999).
- [25] F. H. L. Essler, A. Furusaki, and T. Hikihara, *Phys. Rev. B* **68**, 064410 (2003).
- [26] I. Kuzmenko and F. H. L. Essler, *Phys. Rev. B* **79**, 024402 (2009).
- [27] A. W. Sandvik, *Phys. Rev. B* **57**, 10287 (1998).
- [28] K. S. D. Beach, arXiv e-prints , cond-mat/0403055 (2004), arXiv:cond-mat/0403055 [cond-mat.str-el].
- [29] A. W. Sandvik, *Phys. Rev. E* **94**, 063308 (2016).
- [30] A. W. Sandvik, *J. Phys. A Math. Theor.* **25**, 3667 (1992).
- [31] See the Supplemental Material for details of the QMC-SAC implementation of the quasi-1D quantum magnet, the QMC measurement of dynamic bond correlation function and the detailed discussion on the analytical calculation of the excitation spectra, which includes Refs. [16, 18, 19, 21–24, 29, 32, 42–45].
- [32] H. Shao, Y. Q. Qin, S. Capponi, S. Chesi, Z. Y. Meng, and A. W. Sandvik, *Phys. Rev. X* **7**, 041072 (2017).
- [33] Y. Xu, Z. Xiong, H.-Q. Wu, and D.-X. Yao, *Phys. Rev. B* **99**, 085112 (2019).
- [34] G.-Y. Sun, Y.-C. Wang, C. Fang, Y. Qi, M. Cheng, and Z. Y. Meng, *Phys. Rev. Lett.* **121**, 077201 (2018).
- [35] N. Ma, G.-Y. Sun, Y.-Z. You, C. Xu, A. Vishwanath, A. W. Sandvik, and Z. Y. Meng, *Phys. Rev. B* **98**, 174421 (2018).
- [36] C.-J. Huang, Y. Deng, Y. Wan, and Z. Y. Meng, *Phys. Rev. Lett.* **120**, 167202 (2018).
- [37] N. Ma, Y.-Z. You, and Z. Y. Meng, *Phys. Rev. Lett.* **122**, 175701 (2019).
- [38] Z. Yan, Y.-C. Wang, N. Ma, Y. Qi, and Z. Y. Meng, *npj Quantum Mater.* **6**, 39.
- [39] Y.-C. Wang, M. Cheng, W. Witczak-Krempa, and Z. Y. Meng, arXiv e-prints , arXiv:2005.07337 (2020), arXiv:2005.07337 [cond-mat.str-el].
- [40] Z. Hu, Z. Ma, Y.-D. Liao, H. Li, C. Ma, Y. Cui, Y. Shangguan, Z. Huang, Y. Qi, W. Li, Z. Y. Meng, J. Wen, and W. Yu, *Nat. Commun.* **11**, 5631 (2020).
- [41] Y.-C. Wang, Z. Yan, C. Wang, Y. Qi, and Z. Y. Meng, *Phys. Rev. B* **103**, 014408 (2021).
- [42] A. W. Sandvik, *Phys. Rev. Lett.* **83**, 3069 (1999).
- [43] F. H. L. Essler and R. M. Konik, in *From Fields to Strings: Circumnavigating Theoretical Physics: Ian Kogan Memorial Collection (in 3 Vols)*, Vol. 1, edited by M. Shifman (World Scientific Publishing Co. Pte. Ltd, 2005) pp. 684–830.
- [44] T. Hikihara and O. A. Starykh, *Phys. Rev. B* **81**, 064432 (2010).
- [45] S. Lukyanov and A. Zamolodchikov, *Nucl. Phys. B* **493**, 571 (1997).

SUPPLEMENTAL MATERIAL

Amplitude Mode in Quantum Magnets via Dimensional Crossover

QMC-SAC SCHEME

The relationship between the imaginary-time correlation function of an operator \hat{O} , $G(\tau) = \langle \hat{O}(\tau)\hat{O}(0) \rangle$, and its corresponding spectral function, $A(\omega)$, can be given as

$$G(\tau) = \int_{-\infty}^{\infty} K(\tau, \omega) A(\omega) d\omega, \quad (\text{S1})$$

where the kernel, $K(\tau, \omega)$, depends on the type of the spectral function. For the bosonic case, there is a relation, $A(-\omega) = e^{-\beta\omega} A(\omega)$, between the spectral function at positive and negative frequency. Therefore, we restrict the integral in Eq. (S1) to the positive frequencies by applying the kernel

$$K(\tau) = \frac{1}{\pi} (e^{-\tau\omega} + e^{-(\beta-\tau)\omega}). \quad (\text{S2})$$

From the point of the SAC process, we use the normalization $G(0) = 1$ to work with a spectral function that is itself normalized to unity on the positive frequency axis. Thus, Eq.(S1) becomes

$$G(\tau) = \int_0^{\infty} \frac{e^{\tau\omega} + e^{-(\beta-\tau)\omega}}{1 + e^{-\beta\omega}} B(\omega) d\omega, \quad (\text{S3})$$

where $B(\omega) = A(\omega)(1 + e^{-\beta\omega})$ is the real-frequency spectral function. Hence, $\int_0^{\infty} d\omega B(\omega) = 1$.

Practically, $B(\omega)$ is parameterized by a large number of equal-amplitude δ functions, which is sampled at location in a frequency continuum. The number of δ functions we used are 5000 in both Fig. 2 and Fig. 3. Therefore, $B(\omega) = \sum_{i=0}^{N_\omega-1} a_i \delta(\omega - \omega_i)$. Then, we update location of these δ functions in a Metropolis process using the likelihood function

$$P(B) \propto \exp\left(-\frac{\chi^2}{2\Theta}\right), \quad (\text{S4})$$

where Θ is the sampling temperature. And χ^2 denotes the goodness of fit, which describes the relation between correlation function obtained from QMC measurement, $G(\tau)$, and from Eq. (S3), $G'(\tau)$. χ^2 is defined as

$$\chi^2 = \sum_{i,j} [G'(\tau_i) - \bar{G}(\tau_i)] C_{ij}^{-1} [G'(\tau_j) - \bar{G}(\tau_j)], \quad (\text{S5})$$

where $G'(\tau_i)$ is obtained from the current spectral function by Eq. (S3) and $\bar{G}(\tau_i)$ denotes the statistical average of QMC measurement. C_{ij} is the covariance matrix element of the QMC data

$$C_{ij} = \frac{1}{N_b(N_b - 1)} \sum_{b=1}^{N_b} [G^b(\tau_i) - \bar{G}(\tau_i)][G^b(\tau_j) - \bar{G}(\tau_j)]. \quad (\text{S6})$$

Here N_b refers to the number of bins in the QMC measurement, which is 128 in this study.

Selecting Θ matters in the SAC process. We adopt the temperature-adjustment scheme devised in Ref.[32]. In this scheme, a simulated annealing procedure is used to find the minimum value χ_{min}^2 . After this initial step, Θ is adjusted to make the average χ^2 in the final sampling process for the spectral function satisfy

$$\langle \chi^2 \rangle \approx \chi_{min}^2 + \sqrt{2N_\tau}. \quad (\text{S7})$$

Here N_τ is the size of time point set used in the SAC process, which we will discuss below. With a suitable Θ , a smooth averaged spectral function can be obtained and the final spectral function is the ensemble average of the Metropolis process within the confrontational space of $\{a_i, \omega_i\}$, as explained in Refs. [18, 29].

The spectral function is 'good' when $\langle \chi^2 \rangle$ closes to one. To do so, it is useful to find a suitable time point set $\{G(\tau_i)\}$ that input into the SAC process. Here, those $G(\tau)$ with relative statistic errors larger than 10^{-1} should not be considered in the SAC

process since the ill-posed nature of the inverse Laplace transform. Besides, for a dataset of $G(\tau)$ from the QMC measurement, each time point is chosen and put into the SAC process with the probability

$$P(\tau) = \begin{cases} 1, & \tau = \frac{A_n^2 d\tau}{4} \\ p, & \tau \neq \frac{A_n^2 d\tau}{4} \end{cases} \quad (\text{S8})$$

Here, $d\tau$ is the resolution of $G(\tau)$ in the QMC measurement. And $A_n = \alpha n$ is a sequence of $n = 0, 1, 2, \dots$ and parameter α . $0 < p < 1$ is a constant. By changing parameters α and p , one can construct a suitable $\{G(\tau_i)\}$ and make $\langle \chi^2 \rangle = 1 \pm 0.1$. Finally, we apply $N_\tau \approx 50$ in the SAC process.

FITTING THE EXCITATION GAP

In the Fig. 4 of the main text, we performed finite size scaling of the four different excitation gaps. These gap values are obtained from fitting their normalized imaginary-time correlation function $G(\tau)$ with $G_{\text{fit}}(\tau) = be^{-\omega\tau}$, in which ω refers to the low-energy mode frequency and b is the fitting parameter.

In order to achieve a good fitting, we first find a large τ_{max} with a small relative error (< 0.25) in $G(\tau)$ obtained from QMC. For example, in Fig.S1(a), we prefer $\tau_{\text{max}} = 23.04$, at which the relative error of $G(\tau)$ is 0.224. Secondly, we choose a τ_{min} in $G(\tau)$, which would give a good fitting between τ_{min} and τ_{max} . We use $\tau_{\text{min}} = 5.06$ and obtain $G_{\text{fit}}(\tau) = 0.575e^{-0.306\tau}$, which has been plotted as the blue line in Fig.S1(a). Then, we shift τ_{min} to four closeby imaginary-time points and obtain four other values of ω . For $G_{S^x}(\tau)$ in Fig.S1(a), these four points are $\tau_1 = 4.62$, $\tau_2 = 4.84$, $\tau_3 = 5.29$ and $\tau_4 = 5.52$. Finally, we apply the average over these five different ω as the mode frequency, and their sample standard deviation as the error bar in Fig. 4, which is 0.306 ± 0.028 for A_{S^x} with $g = 0.1$, $h = 0$ and system size $L = 36$ at $\mathbf{k} = (\pi, \pi/2)$. With this method, we have also plotted the normalized imaginary-time correlation functions of spin (or bond) operator and our fitting results in Fig.S1.

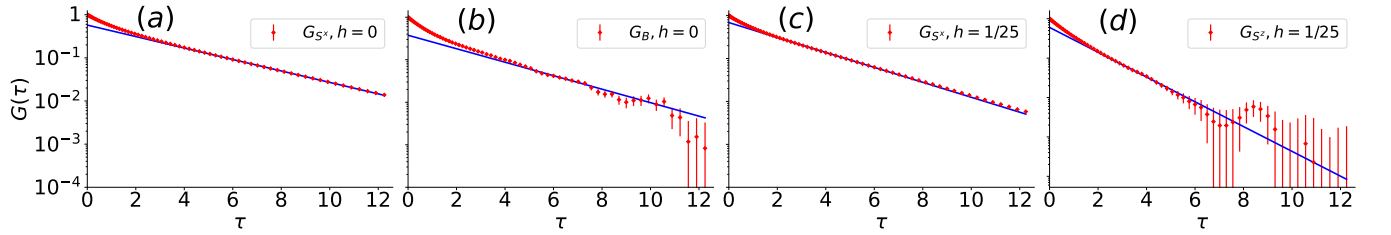


FIG. S1. Scheme of the imaginary-time correlation fitting. (a-d) show the normalized imaginary-time correlation of corresponding operator respectively [$G_{S^z}(\tau)$, $G_B(\tau)$, $G_{S^z}(\tau)$ and $G_{S^x}(\tau)$], with $g = 0.1$ and system size $L = 36$ at $\mathbf{k} = (\pi, \pi/2)$. The red dots are QMC data and the blue lines are our fitting curves.

BOND-BOND CORRELATION MEASUREMENT

To measure the bond-bond correlation G_B (the scalar mode), we design the follow correlation functions, by using O_3 spin-rotational symmetry,

$$\begin{aligned} G_B(i-j, \tau) &= \langle B_i(\tau) B_j(0) \rangle \\ &= \langle [\mathbf{S}_{i+\hat{x}}(\tau) \cdot \mathbf{S}_i(\tau)] [\mathbf{S}_{j+\hat{x}}(0) \cdot \mathbf{S}_j(0)] \rangle \\ &= 3 \langle [S_{i+\hat{x}}^z(\tau) S_i^z(\tau)] [S_{j+\hat{x}}^z(0) \cdot \mathbf{S}_j(0)] \rangle \\ &= 3 \langle S_{i+\hat{x}}^z(\tau) S_i^z(\tau) S_{j+\hat{x}}^z(0) S_j^z(0) \rangle + \frac{3}{2} \langle [S_{i+\hat{x}}^z(\tau) S_i^z(\tau)] [S_{j+\hat{x}}^+(0) S_j^-(0) + S_{j+\hat{x}}^-(0) S_j^+(0)] \rangle \\ &= 3 \langle B_i^z(\tau) B_j^z(0) \rangle + 3 \langle B_i^z(\tau) B_j^\pm(0) \rangle \\ &= 3G_{B^z}(i-j, \tau) + 3G_{B^\pm}(i-j, \tau). \end{aligned} \quad (\text{S9})$$

Here, $B_i^z = S_{i+\hat{x}}^z S_i^z$ and $B_i^\pm = \frac{1}{2}(S_{i+\hat{x}}^+ S_i^- + S_{i+\hat{x}}^- S_i^+)$ are the longitudinal and transverse components of the bond-bond correlation. As shown in Eq. (S9), G_B contains two different parts, which are the diagonal term $G_{B^z}(i-j, \tau) = \langle B_i^z(\tau) B_j^z(0) \rangle$ and the cross

term $G_{B^z}(i-j, \tau) = \langle B_i^z(\tau) B_j^z(0) \rangle$. When applying the $\{S^z\}$ basis in SSE-QMC simulation [21–23], the measurement of the G_{B^z} term is simple since it is also in the eigenbasis of the B_i^z operator. For a given static configuration space, one can calculate the value of B_i^z directly. However, the measurement of the cross term G_{B^z} is difficult, since the $\{S^z\}$ basis is not the eigenbasis of B_i^z and the cross term measurement cannot be directly applied in a given static configuration space. In fact, in the previous QMC works about the measurement of bond-bond correlations, it is usually the G_{B^z} term that has been measured [18, 19], for the sake of simplicity as mentioned above.

However, in our case of the coupled spin chains, we have seen that the measurement of G_{B^z} will mix with the phase mode of spin wave and generate additional spurious features close to the Γ point (although the breather mode between $M \rightarrow X_1$ close to the 1D limit is kept intact), and it is only in the full measurement of $G_{B^z} + G_{B^z}$, including the contribution of the cross term, that the true scalar mode spectra are revealed. Below we explain how such full measurement of G_B is implemented in the QMC simulation.

To measure the cross term, it is convenient to bring our attention back to the updates of configuration spaces in the SSE-QMC simulation. There are two important updates, the diagonal update and the directed loop update. The former is about inserting and removing the diagonal operators in the configuration spaces while the latter can be viewed as the creation, annihilation, and movement of the off-diagonal operator in the configuration space. For example, in our model, the Hamiltonian (Eq. (1)) only includes two kinds of off-diagonal term, $S_i^+ S_j^-$ and $S_i^- S_j^+$. Hence, the directed loop update process can be understood as follows. A pair of off-diagonal operators, S_i^+ and S_i^- , are created on a random site i at a random time τ in the configuration space. One of the operators is fixed while the other moves in the configuration space according to the detailed balance condition. When these two operators meet each other again, they annihilate and the loop is constructed. Therefore, within this picture, to measure the correlation about S_i^+ and S_i^- is about tracing the movement of off-diagonal operators in the configuration space when constructing loops in the directed loop update process.

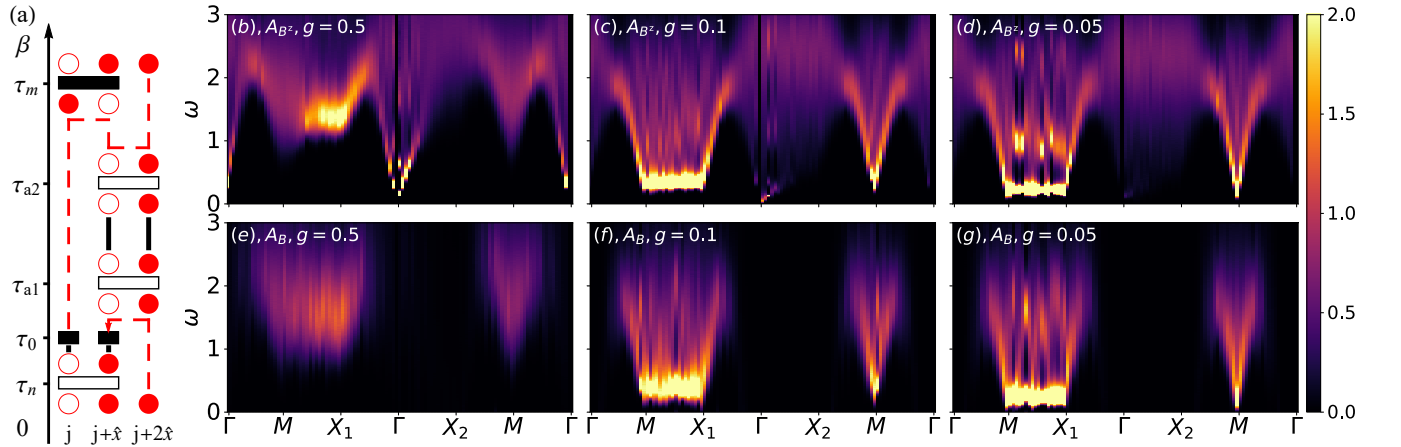


FIG. S2. (a) The schematic diagram of the cross term G_{B^z} measurement in the configuration space of SSE-QMC simulation. The red solid (hollow) circle refers to the spin up (down). And the big solid (hollow) rectangles is the (off-)diagonal operator, such as $S_i^z S_j^z$ for diagonal and $S_i^+ S_j^-$ for off-diagonal. The two small rectangles is the pair of operator created in the directed loop update process and the red dashed line is the path of the moving operator. Also, we plot the imaginary time axis pointing from 0 to β , and map each operator to a space-time coordinate (like (i, τ_0)). (b), (c), (d) and (e), (f), (g) show the spectra function of bond operators respectively, $A_{B^z}(\mathbf{q}, \omega)$ and $A_B(\mathbf{q}, \omega)$ at $h = 0$, at different values of $g = J/J_\perp$, with the system size $L = 36$ and inverse temperature $\beta = 4L$.

In practice, starting from a given configuration space with N_h operators, we first map N_h operators to N_h sorted random imaginary time point between 0 and β . For example, as in Fig. S2 (a), there are four bond operators. Hence, we map them to four imaginary time point, which are $\tau_n, \tau_{a1}, \tau_{a2}$, and τ_m . Noted that each imaginary time point is selected randomly but fulfill that $0 \leq \tau_n < \tau_{a1} < \tau_{a2} < \tau_m \leq \beta$. Therefore, one can deduce the spin state in the configuration space for a given τ . When measuring the pure term G_{B^z} , we select a imaginary time point τ_0 randomly in the configuration space. And then, we deduce the corresponding spin state at τ_0 and $\tau_0 + \tau$ in the configuration space, and calculate the value of $\langle B_i^z(\tau) B_j^z(0) \rangle$. With a large number of sampling ($\approx 10^4$ Monte Carlo step), the final result of G_{B^z} is given as the average.

For the cross term measurement, within the directed loop update in SSE-QMC simulation, we first select a vertex leg in the configuration space randomly. Then, we create a pair of off-diagonal operators at the random point (j, τ_0) on this vertex leg. For example, in Fig. S2(a), S_j^+ and S_j^- are created at (j, τ_0) , which is on the vertex leg connecting the operators at τ_n and τ_m . Since τ_0 here is selected randomly in the region $[\tau_n, \tau_m]$ instead of $[0, \beta]$, the creation here causes a weight $w_{mn}^l = \text{mod}[(\tau_m - \tau_n), \beta]$ in our measurement, where l is the index of constructing loop and mod calculation comes from the periodic boundary condition in

the imaginary time.

Then, we fix one of the inserted operators and move the other according to the detail balance condition. Meanwhile, we trace the path of the moving operator and monitor whether it arrives the point $(j + \hat{x}, \tau_0)$. If the moving operator arrives the point $(j + \hat{x}, \tau_0)$ (as in Fig.S2(a) with the periodic boundary condition in time), we pause the construction of the loop and measure the $B_i^z(\tau)$ relative to (j, τ_0) in the current configuration space, in which the measurement result are recorded as $g^l(i - j, \tau)$ and l is the loop index. If the moving operator never meets $(j + \hat{x}, \tau_0)$, it means that $S_j^+ S_{j+\hat{x}}^-$ or $S_j^- S_{j+\hat{x}}^+$ does not appear in the current loop construction. Therefore, the measurement result $g^l(i - j, \tau) = 0$. If the moving operator meet the fixed one, they annihilate and directed loop update completes. With large enough samplings ($\approx 10^4 L$ loops in our simulation), the final measurement result of cross term can be read as

$$G_{B^c}(i - j, \tau) = \frac{\sum_l w_{mn}^l g^l(i - j, \tau)}{\sum_l w_{mn}^l}. \quad (\text{S10})$$

where the weights w_{mn}^l is given above. In this way, both G_{B^z} and G_{B^c} are measured in the SSE-QMC and we obtain the full bond-bond correlation function as in Eq. (S9).

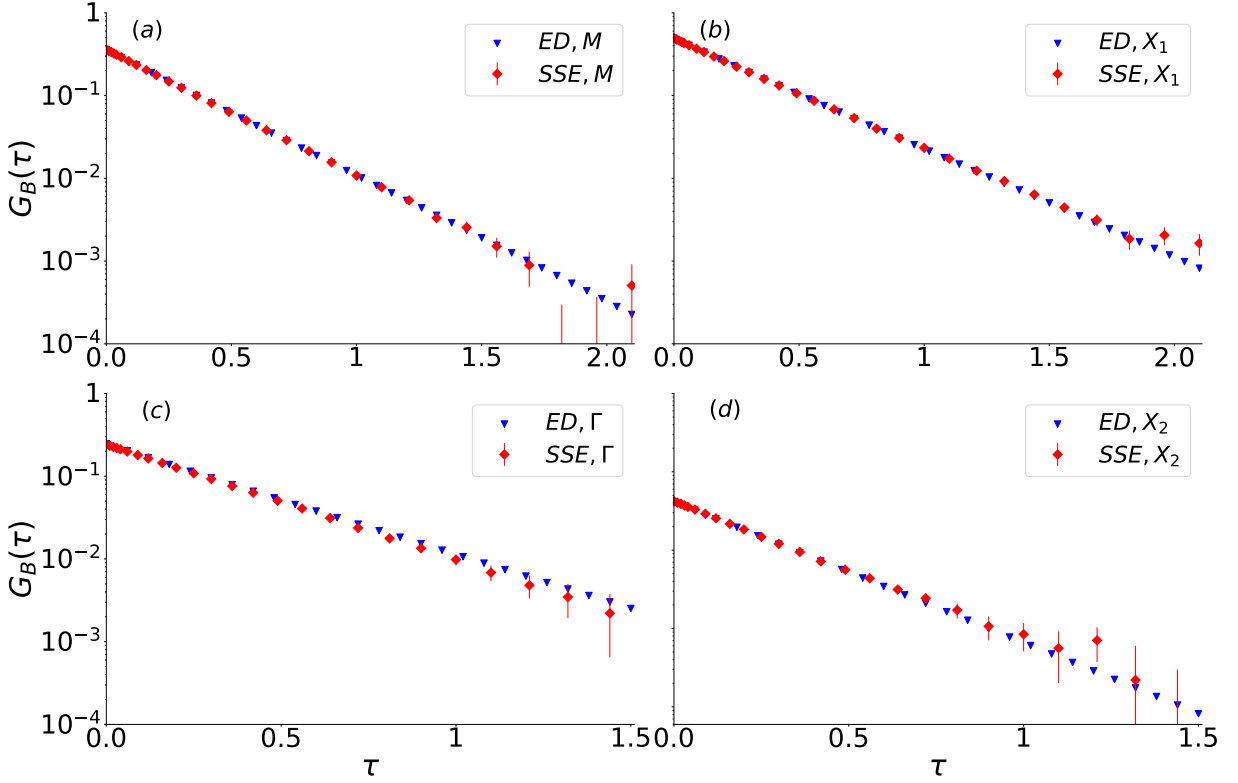


FIG. S3. Comparison of the dynamic bond correlation from exact diagonalization and QMC simulation as a function of imaginary time, the system parameters are $L = 4$, $h = 0$ and $g = 1$ for $G_B(\tau)$ at (a) M , (b) X_1 , (c) Γ and (d) X_2 momenta.

To make sure the measurement of the dynamic bond correlation is correct, we first compare the imaginary time results with the same measurements from the exact diagonalization (ED), and the comparison is shown in Fig. S3. This is a small system with $L = 4$ and we plot the imaginary time decay of the full dynamic bond correlation at four momenta ($G_B(\Gamma, \tau)$, $G_B(X_1, \tau)$, $G_B(X_2, \tau)$ and $G_B(M, \tau)$), the ED imaginary time results are obtained from the Fourier transformation of Matsubara correlation function obtained by continued fraction expansion using Lanczos method. The match is perfect within Monte Carlo statistical errors.

Meanwhile, in Fig. S2 (b) - (g), we show the comparison of the spectral functions of bond-bond correlation A_B (A_{B^c}) in B (B^z) channels, respectively. It is clear that the main difference between A_B and A_{B^c} comes from the region close to Γ points in Fig.S2, especially at the 2D limit with $g = 0.5$. In A_{B^c} (Fig. S2 (b) and (c)), it shows a gapless mode at Γ points, this is due to the mixing between the B^z and the phase mode of S^z . And such artificial features disappear only the cross term B^c is properly taken into the measurement and does not exist in A_B (Fig. S2 (e) and (f)). Although the first breather at the 1D limit between $M \rightarrow X_1$ are similar in Fig. S2 (d) and (g) with $g = 0.05$, in the main text, we use the full bond-bond correlation as the correct measurement.

FIELD THEORY TREATMENT

In this section, we discuss the theoretic treatment, where the interchain coupling is treated within a mean-field and random-phase approximation while the intrachain (1D) physics are treated via bosonization and exact methods. For more details about this theory approach, see the review by Essler and Konik [43] and reference therein. In comparison with Ref. 43, here it is needed to generalize the theory analysis a bit in order to incorporate the external staggered field utilized in the simulations.

Here, we will set the temperature $T = 0$ and the system size $L = \infty$. Without loss of generality, we set the AFM order to be along the S^z direction with an order parameter $m_0 = (-1)^i \langle S_i^z \rangle$.

Self-consistent Mean-field Treatment

Here, we start from taking the self-consistent mean-field treatment for the interchain couplings ($J_\perp \sum_{\langle i,j \rangle_y} \mathbf{S}_i \cdot \mathbf{S}_j$), while quantum fluctuations around the mean-field ground state will be considered later via a random-phase approximation (RPA). Within the mean-field treatment, $\langle S_i^z \rangle = m_0 (-1)^i$ and thus this interchain coupling turns into an effective staggered field for each spin chain (h_{eff}) with a mean-field Hamiltonian

$$H_{MF} = J \sum_{\langle i,j \rangle_x} \mathbf{S}_i \cdot \mathbf{S}_j - (h + h_{\text{eff}}) \sum_i (-1)^i S_i^z, \quad (\text{S11})$$

where

$$h_{\text{eff}} = 2J_\perp m_0. \quad (\text{S12})$$

and h is the external staggered field.

For this mean-field Hamiltonian, the 1D spin chains decouple from each other, and thus it can be solved via 1D exact/non-perturbative methods. At low-energy, the mean-field Hamiltonian of each spin chain can be reduced to the quantum sine-Gordon (SG) model via bosonization with an Hamiltonian

$$H_{SG} = \int dx \left\{ \frac{v}{16\pi} [(\partial_x \Phi)^2 + (\partial_x \theta)^2] - \mu \cos(\beta \Phi) \right\} \quad (\text{S13})$$

where $\beta = 1/2$, $v = \pi J a_0/2$, and $\mu = c(h + h_{\text{eff}})a_0^{-1/2}$. The constant c here is $1/2$ and a_0 is the lattice constant, which will be set to unity ($a_0 = 1$). In this bosonized form, the spin S_i^z operator becomes

$$S_i^z \sim \frac{\partial_x \Phi}{4\pi} + c(-1)^i \cos(\Phi/2), \quad (\text{S14})$$

and the expectation value of the order parameter is $m_0 = (-1)^i \langle S_i^z \rangle = c \langle \cos(\Phi/2) \rangle$. This expectation value was evaluated in Ref. 45 and is given by

$$m_0 = \frac{(2\pi J/v)^{1/3}}{6\sqrt{3}} \left[\frac{\Gamma(\frac{3}{4})}{\Gamma(\frac{1}{4})} \right]^{4/3} \left[\frac{\Gamma(\frac{1}{6})}{\Gamma(\frac{2}{3})} \right]^2 \left(\frac{h + h_{\text{eff}}}{J} \right)^{1/3} \quad (\text{S15})$$

Because $h_{\text{eff}} = 2J_\perp m_0$, Eqs. (S12) and (S15) enforce a self-consistency condition for h_{eff}

$$\frac{h_{\text{eff}}}{J} = \gamma_1 \frac{J_\perp}{J} \left(\frac{h + h_{\text{eff}}}{J} \right)^{1/3}, \quad (\text{S16})$$

where the coefficient

$$\gamma_1 = \frac{2^{2/3}}{3\sqrt{3}} \left[\frac{\Gamma(\frac{3}{4})}{\Gamma(\frac{1}{4})} \right]^{4/3} \left[\frac{\Gamma(\frac{1}{6})}{\Gamma(\frac{2}{3})} \right]^2 \approx 1.215340 \quad (\text{S17})$$

Here, we used the fact that $v/J = \pi/2$. By solving cubic equation (S16), the value of the effective staggered field (h_{eff}) can be determined

$$h_{\text{eff}} = \frac{3h}{x} \cos\left(\frac{\arccos x}{3}\right) \quad (\text{S18})$$

where

$$x = \frac{3\sqrt{3}}{2} \frac{h/J}{(\gamma_1 \frac{J}{J})^{3/2}} = \frac{3\sqrt{3}}{2} \frac{h/J}{(\gamma_1 g)^{3/2}} \quad (\text{S19})$$

Notice that Eq. (S18) is defined for $x \leq 1$ (weak field) due to the utilization of $\arccos x$. To extend it to $x > 1$ (strong field), one can just replace $\cos(\arccos(x)/3)$ with its analytic continuation $\cosh(\text{arccosh}(x)/3)$. In the absence of external field $h = 0$, the equation above reduces to $h_{\text{eff}} = (\gamma_1 g)^{3/2} J$.

Given relatively short chains used in our numerical study, $L = 20-36$, the derivation above does not account for the logarithmic corrections to the mass gap and other quantities. These corrections arise due to the marginally irrelevant interaction of chiral spin currents [24, 43] and become important in the long chain limit [42].

1D Spectral Functions

In this section, we compute the spectrum function of spin-spin and bond-bond correlators for the 1D mean-field Hamiltonian, ignoring any inter-chain quantum fluctuations, which will be studied in the next section. In the bosonized form, the SG model described above (with $\beta = 1/2$) contains four gapped excitations. In notations of [43] here $\xi = 1/3$. Three of them (soliton, anti-soliton and the first breather B_1) shares the same energy gap Δ , while the last one (i.e., the second breather B_2) has a larger gap $\sqrt{3}\Delta$. The mass Δ_n of the n -th breather is determined as

$$\Delta_n = 2\Delta \sin\left(\frac{\pi\xi n}{2}\right) = 2\Delta \sin(\pi n/6) \quad (\text{S20})$$

so that $\Delta_1 = \Delta$ (mass of the first breather coincides with that of the soliton and antisoliton), $\Delta_2 = \sqrt{3}\Delta$ (mass of the second breather) and $\Delta_3 = 2\Delta$ (mass of the third breather, coincides with the boundary of the soliton-antisoliton continuum).

And the value of the gap Δ is

$$\frac{\Delta}{J} = \sqrt{\pi} \left(\frac{v}{\pi J/2}\right) \frac{\Gamma(\frac{1}{6})}{\Gamma(\frac{2}{3})} \left[c \left(\frac{\pi J/2}{v}\right) \frac{\Gamma(\frac{3}{4})}{\Gamma(\frac{1}{4})} \frac{h + h_{\text{eff}}}{J} \right]^{2/3} \quad (\text{S21})$$

Because $v = \pi J/2$ and $c = 1/2$, we have

$$\frac{\Delta}{J} = \frac{3^{3/4}\pi^{1/2}}{2} \gamma_1^{1/2} \left(\frac{h + h_{\text{eff}}}{J}\right)^{2/3} \quad (\text{S22})$$

Here, we substitute h_{eff} with the solution of Eq. (S18)

$$\frac{\Delta}{J} = \frac{3^{3/4}\pi^{1/2}}{2} \gamma_1^{1/2} \left(\frac{h}{J}\right)^{2/3} \left[1 + \frac{3}{x} \cos\left(\frac{\arccos x}{3}\right) \right]^{2/3} \quad (\text{S23})$$

where the value of x can be computed via Eq. (S19). This formula gives the gap of excitations, as a function of control parameters h and g . Most importantly, here we define two quantities Δ_0 and b_h . Δ_0 is the gap value in the absence of external field

$$\frac{\Delta_0}{J} = \frac{\Delta(h=0)}{J} = \frac{3^{3/4}\pi^{1/2}}{2} \gamma_1^{3/2} g \quad (\text{S24})$$

where $\gamma_1 \approx 1.215340$ as defined in Eq. (S17). b_h is a dimensionless quantity characterizing the field dependence $b_h = \left(\frac{\Delta}{\Delta_0}\right)^2 - 1$, where, Δ is the the value of the gap in the presence of an external field (h) and it is normalized by the zero-field gap value (Δ_0). By definition, b_h is a function of the field h and its value vanishes at $h = 0$. From Eq. (S23), it is easy to check that

$$b_h = \frac{(h/J)^{4/3}}{\gamma_1^2 g^2} \left[1 + \frac{3}{x} \cos\left(\frac{\arccos x}{3}\right) \right]^{4/3} - 1 \quad (\text{S25})$$

with x defined in Eq. (S19)

The spin-spin and bond-bond correlation functions are

$$\langle S_i^x(t) S_j^x(t') \rangle = \langle S_i^y(t) S_j^y(t') \rangle \simeq c^2 (-1)^{i-j} \left\langle \sin\left(\frac{\Theta(x_i, t)}{2}\right) \sin\left(\frac{\Theta(x_j, t')}{2}\right) \right\rangle \quad (\text{S26})$$

$$\langle S_i^z(t) S_j^z(t') \rangle \simeq c^2 (-1)^{i-j} \left\langle \cos\left(\frac{\Phi(x_i, t)}{2}\right) \cos\left(\frac{\Phi(x_j, t')}{2}\right) \right\rangle \quad (\text{S27})$$

$$\langle B_i(t) B_j(t') \rangle \propto \left\langle \sin\left(\frac{\Phi(x_i, t)}{2}\right) \sin\left(\frac{\Phi(x_j, t')}{2}\right) \right\rangle \quad (\text{S28})$$

where $x_i = ia_0$ and $x_j = ja_0$ are the spatial coordinate of the the spin/bond. It is worthwhile to emphasize here that in the AFM phase ($m_0 \neq 0$) with an order parameter along the S^z direction, although the bond operator B and S^z share the same symmetry, the bond operator spectrum is characterized the same mass as that of S^x and S^y operators, and is different from that of S^z . This fact will lead to a key consequence. As will be shown below, it implies that the $B - B$ correlator and the $S^z - S^z$ correlator are probing different excitations in quasi-1D systems. This is in sharp contrast to higher dimensions, where the two correlators can both be used to probe the amplitude mode due to their identical symmetry.

These 1D correlation functions can be calculated. For k_x near π , we have

$$\tilde{\chi}_{S^x}(\omega, k_x) = \frac{Z_1}{\omega^2 - v^2(k_x - \pi)^2 - \Delta^2 + i\delta} + \text{incoherent background} \quad (\text{S29})$$

$$\tilde{\chi}_{S^z}(\omega, k_x) = \frac{Z_2}{\omega^2 - v^2(k_x - \pi)^2 - 3\Delta^2 + i\delta} + \text{incoherent background} \quad (\text{S30})$$

$$\tilde{\chi}_B(\omega, k_x) = \frac{Z_3}{\omega^2 - v^2(k_x - \pi)^2 - \Delta^2 + i\delta} + \text{incoherent background} \quad (\text{S31})$$

where Δ is the soliton energy [Eq. (S23)]. If the external field is turned off ($h = 0$), Δ recovers the zero-field value Δ_0 , as shown in Eq. (S24). Here, we only shows the coherent modes, while the incoherent background (the continuum) are ignored. Because the continuum only appear for $\omega \geq 2\Delta$ while the frequency of the coherent modes ($\omega = \Delta$ and $\omega = \sqrt{3}\Delta$) are all below 2Δ , the continuum can be ignored as far as these low-energy excitations are concerned. As already mentioned above, the coherent modes of S^x and the bond operator shares the same dispersion and energy gap (Δ), while S^z mode have a larger gap $\sqrt{3}\Delta$.

Random Phase Approximation and 2D Susceptibilities

In the previous section, we presented the dynamical susceptibilities of the spin/bond operators ($\tilde{\chi}$). In this section, 2D dynamical susceptibility will be computed via a random phase approximation (RPA). To distinguish 1D and 2D dynamical susceptibilities, 1D and 2D susceptibilities will be represented by $\tilde{\chi}$ and χ (with and without tilde on top) respectively.

Within the RPA approximation, 2D dynamical susceptibilities for S^x and S^z are

$$\chi_{S^x} = \frac{1}{(\tilde{\chi}_{S^x})^{-1} - 2J'(k_y)} \quad (\text{S32})$$

$$\chi_{S^z} = \frac{1}{(\tilde{\chi}_{S^z})^{-1} - 2J'(k_y)} \quad (\text{S33})$$

where $J'(k_y) = J_\perp \cos k_y$ is the Fourier transform of the inter-chain coupling. As for the bond-bond correlation function, because the interchain bond-bond coupling comes from second-order (and higher-order) perturbation in $g \ll 1$, the interchain coupling constants scales as J_\perp^2/J and thus is small for weak J_\perp , $J_\perp^2/J \ll J_\perp$ [44]. As a result, to the leading order, the bond-bond correlation does not receive any corrections within the RPA approximation, and therefore

$$\chi_B = \tilde{\chi}_B \quad (\text{S34})$$

In summary, we find

$$\chi_{S^x}(\omega, \mathbf{k}) = \chi_{S^y}(\omega, \mathbf{k}) = \frac{Z_1}{\omega^2 - v^2(k_x - \pi)^2 - (\Delta^2 + 2Z_1 J_\perp \cos k_y) + i\delta} \quad (\text{S35})$$

$$\chi_{S^z}(\omega, \mathbf{k}) = \frac{Z_2}{\omega^2 - v^2(k_x - \pi)^2 - (3\Delta^2 + 2Z_2 J_\perp \cos k_y) + i\delta} \quad (\text{S36})$$

$$\chi_B(\omega, \mathbf{k}) = \frac{Z_3}{\omega^2 - v^2(k_x - \pi)^2 - \Delta^2 + i\delta} \quad (\text{S37})$$

From the Goldstone theorem, we know that at $h = 0$, in the SSB phase the phase fluctuations mode χ_{S^x} shall be gapless at $k_y = \pi$. This condition fixes the value of Z_1

$$\Delta_0 = \sqrt{2Z_1 J_\perp}. \quad (\text{S38})$$

Because 1D exact methods fix the ratio between Z_1 and Z_2 , $Z_2/Z_1 \approx 0.491309$ [16], the value of Z_2 is also determined. As for Z_3 , because its value doesn't change the mode frequency, it will not be evaluated here.

As a result, the dispersion of these three modes are

$$\omega_{S^x} = \omega_{S^y} = \Delta_0 \sqrt{1 + b_h + \cos k_y + \frac{v^2(k_x - \pi)^2}{\Delta_0^2}} \quad (\text{S39})$$

$$\omega_{S^z} = \Delta_0 \sqrt{3(1 + b_h) + \frac{Z_2}{Z_1} \cos k_y + \frac{v^2(k_x - \pi)^2}{\Delta_0^2}} \quad (\text{S40})$$

$$\omega_B = \Delta_0 \sqrt{1 + b_h + \frac{v^2(k_x - \pi)^2}{\Delta_0^2}} \quad (\text{S41})$$

where Δ_0 is the value of Δ in the absence of external field [Eq. (S24)] and the dimensionless parameter b_h is function of the field strength, defined in Eq. (S25). The ratio $Z_2/Z_1 \approx 0.491309$. The velocity along the chain is $v = \pi J/2$ as shown above.

At $k_x = \pi$ and in the absence of external field ($h = 0$ and thus $b_h = 0$), the dispersion relations become

$$\omega_{S^x} = \omega_{S^y} = \Delta_0 \sqrt{1 + \cos k_y} \quad (\text{S42})$$

$$\omega_{S^z} = \Delta_0 \sqrt{3 + \frac{Z_2}{Z_1} \cos k_y} \quad (\text{S43})$$

$$\omega_{S^B} = \Delta_0 \quad (\text{S44})$$

And it is easy to check that near $k_x = \pi$, for any values of k_y , the frequency of these modes never reach 2Δ , which is the onset frequency, above which the 1D incoherent continuum start to arise. This fact justifies the procedure above, where we dropped the incoherent background in $\tilde{\chi}$. In addition, this observation also implies that these modes are lightly damped at small J_\perp (i.e., the damping only comes from interchain fluctuations), which is the key reason why they leads to clear peaks in the spectrum functions.

AMPLITUDE AND PHASE MODES FROM QMC MEASUREMENTS

In this section, we show that in the absence of the staggered pinning field (h), the spin-spin correlation measured in QMC simulations shall reveal information about both phase and amplitude fluctuations.

Because spontaneous symmetry breaking only arises in the thermodynamic limit, while QMC simulations are performed with finite-size systems, all measurements in such finite-size simulations shall exhibit the full symmetry of the Hamiltonian (without spontaneous symmetry breaking) in both ordered and disordered phase. For example, in a model with Heisenberg spins, (i.e. the model studied in this manuscript), the spin-spin correlation function measured in QMC simulations will always exhibit the SO(3) symmetry, unless a pinning field h is introduced to explicitly break this symmetry.

This absence of spontaneous symmetry breaking is a finite-size effect. Same as most other finite-size effects, it implies that finite-size analysis and extrapolation are required, in order to access the thermodynamic limit. However, as will be shown below, this particular finite-size effect, i.e., the absence of spontaneous symmetry breaking, provides a tool to access both phase and amplitude fluctuations in one single correlation function, in contrast to the thermodynamic limit, where information about the amplitude and phase modes are encoded in different components of spin fluctuations, parallel and perpendicular to the direction of the magnetic order respectively.

In the ordered phase, because of the finite size, QMC simulations will sample the entire phase space, instead of just one ordered state. When the system size is large enough (but still finite), this effect can be characterized via the density matrix, which takes the following form to the leading order

$$\rho = \sum_{\vec{n}} \rho_{\vec{n}} + \dots, \quad (\text{S45})$$

Here, ρ is the density matrix of QMC simulations, which samples all possible configurations. $\rho_{\vec{n}}$ is the restricted density matrix, limited to sample only configurations around one of the ordered states, whose order parameter is aligned to the \vec{n} direction, with \vec{n} being a 3D unit vector. The sum here is performed over all possible direction of \vec{n} . The \dots represent higher order terms, e.g. cross terms between two different ordered states, which vanishes in the thermodynamic limit. For simplicity, here we will ignore all such higher order terms, and only focus on the leading contribution $\sum_{\vec{n}} \rho_{\vec{n}}$.

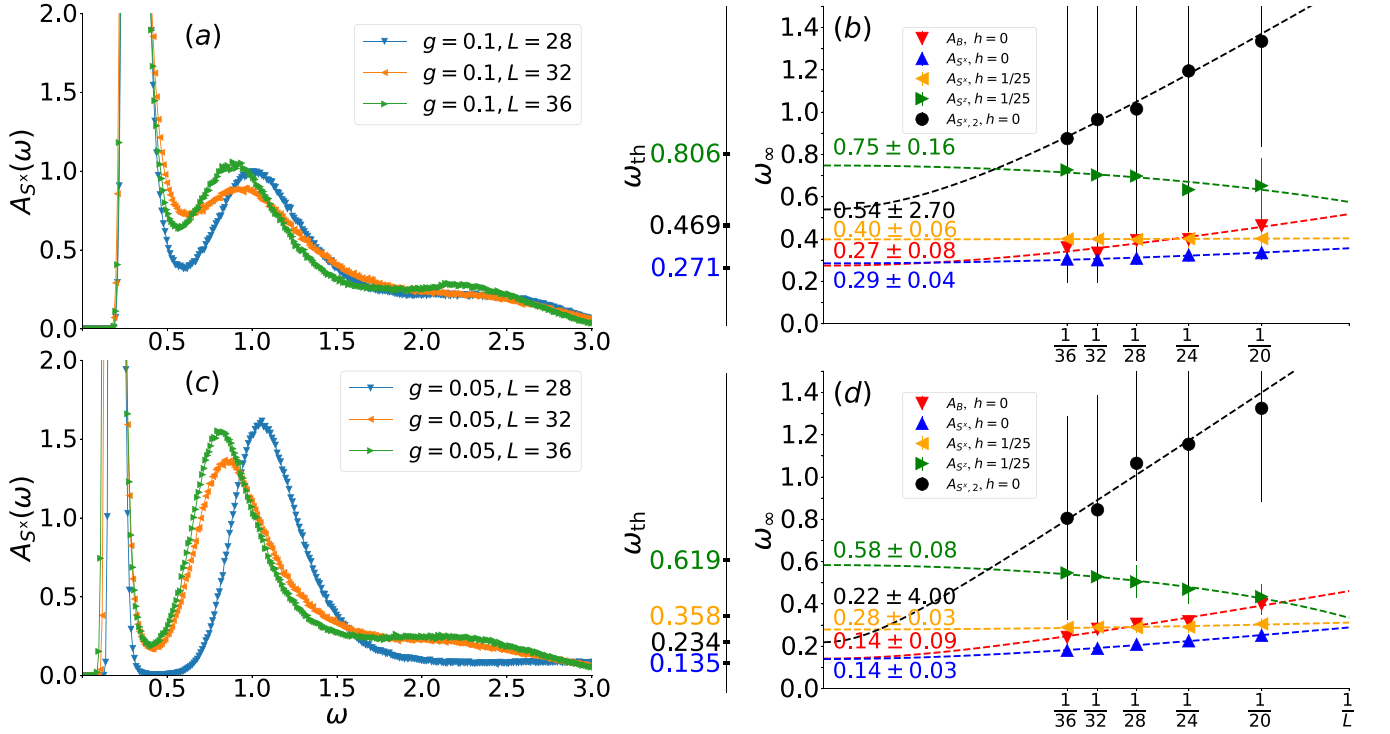


FIG. S4. Frequency dependence of the spectral functions at $\mathbf{k} = (\pi, \pi/2)$ for $A_S^x(\omega)$ with $h = 0$ for (a) at $g = 0.1$ and (c) at $g = 0.05$. And finite-size analysis for (b) $g = 0.1$ and (d) $g = 0.05$ at the same momentum point. The vertical ω_∞ -axis shows extrapolation of the numerical data to the $L = \infty$ limit. Values on the vertical ω -axis mark analytical predictions for the peak frequencies of different modes. See text for details.

For a real physical system in the thermodynamic limit, only a single $\rho_{\vec{n}}$ will be selected in the ordered phase, due to spontaneous symmetry breaking. However, for finite-size systems, all $\rho_{\vec{n}}$'s will contribute to the ensemble average with the same probability, as shown in Eq. (S45). As a result, if we measure a correlation function in the ordered phase, e.g., $\langle S_i^x S_j^x \rangle$, it shall get signals from all possible symmetry breaking states

$$\langle S_i^x S_j^x \rangle_{\text{QMC}} = \frac{1}{Z} \sum_{\vec{n}} \text{tr}(\rho_{\vec{n}} S_i^x S_j^x), \quad (\text{S46})$$

where the normalization factor Z is the partition function. Due to the SO(3) rotational symmetry, we can rewrite this formula as

$$\langle S_i^x S_j^x \rangle_{\text{QMC}} = \frac{1}{Z} \sum_{\vec{n}} \text{tr}(\rho_{\vec{z}} S_i^{\vec{n}} S_j^{\vec{n}}), \quad (\text{S47})$$

In Eq. (S46), we fix the direction of the spin (S^x) and let the direction of the order parameter to rotate and to explore all possible solid angle. In Eq. (S47), instead, we rotate the direction of the spin $S^{\vec{n}}$ with a fixed direction for the order parameter ($\rho_{\vec{z}}$, i.e. the order parameter is along the z direction). Due to the rotational symmetry, these two options are fully equivalent, once we sum over all possible solid angle $\sum_{\vec{n}}$.

With proper normalization factor, $\sum_{\vec{n}} S_i^{\vec{n}} S_j^{\vec{n}} = (S_i^x S_j^x + S_i^y S_j^y + S_i^z S_j^z)/3$, we therefore get

$$\langle S_i^x S_j^x \rangle_{\text{QMC}} = \frac{1}{3} (\langle S_i^x S_j^x \rangle_z + \langle S_i^y S_j^y \rangle_z + \langle S_i^z S_j^z \rangle_z), \quad (\text{S48})$$

where $\langle \dots \rangle_{\text{QMC}}$ represents the expectation value obtained from QMC simulations with contributions from all possible ordered states, and $\langle \dots \rangle_z$ is the expectation value from only one ordered state with the order parameter aligned to the z direction. Here, it is easy to realize that $\langle S_i^x S_j^x \rangle_z$ and $\langle S_i^y S_j^y \rangle_z$ measure phase fluctuations perpendicular to the order parameter, while $\langle S_i^z S_j^z \rangle_z$ gives amplitude fluctuations with spin along the order parameter direction. Thus, in QMC simulations, $\langle S_i^x S_j^x \rangle_{\text{QMC}}$ shall contain signals from both channels, phase and amplitude. This is the reason why we can see both these two modes in this one single correlation function in QMC.

For a regular 2D system with magnetic order, although $\langle S_i^x S_j^x \rangle_{\text{QMC}}$ in principle could detect both phase and amplitude fluctuations, the amplitude contribution will typically be buried in the incoherent background of phase fluctuations. This is because in a typical 2D magnet, amplitude fluctuations are strongly damped and the characteristic frequency range of such strongly damped fluctuations coincide with incoherent background of the phase fluctuations. As a result, we may add contributions from both phase and amplitude fluctuations in Eq. (S48), no clear signature of the amplitude part shall be observed. This is in good agreement with existing QMC studies as well as the 2D limit with $g = 0.5$ showed in the main text. However, in the quasi-1D limit, the sharp and strong amplitude mode shall give a clear feature in the QMC measurement, as shown in the main text. This physics (where one observe both the phase and amplitude mode via $\langle \dots \rangle_{\text{QMC}}$) is highly generic and in principle it shall arise in any systems where a strong and under-damped amplitude mode emerges.

In practice, in order to detect the amplitude mode via $\langle S_i^x S_j^x \rangle_{\text{QMC}}$, it needs to first convert imaginary time (Matsubara frequency) QMC measurements to real time (real frequency) via analytical continuation. Then, in the real-frequency spectral function A_{S^x} , one shall observe two peaks: the phase mode at a lower frequency and the amplitude mode at a higher frequency. This is exactly what observed in our simulations at quasi 1D (small g) as shown in Fig. S4, where we plot A_{S^x} at $k = (\pi, \pi/2)$ at $h = 0$. From the figure, two clear features (peaks) emerge in the quasi-1D limit (small g).

From the QMC data, the second, higher-energy peak in A_{S^x} (denoted as $A_{S^x,2}$ in Fig. S4) is much broader than the lowest peak. This is mostly due to inherent difficulty of analytical continuation. By definition, a real-frequency mode at frequency ω manifests itself as an exponential decay in imaginary time with decay rate ω , i.e., real frequency oscillations $Ae^{-i\omega t}$ implying a decay in the corresponding imaginary-time correlation function $Ae^{-\omega\tau}$. Thus, if we have multiple modes in real time/frequency, the imaginary-time correlation function shall exhibit multiple exponential decays, i.e.

$$A_1 e^{-i\omega_1 t} + A_2 e^{-i\omega_2 t} + \dots \Leftrightarrow A_1 e^{-\omega_1 \tau} + A_2 e^{-\omega_2 \tau} + \dots \quad (\text{S49})$$

In the presence of multiple exponential decay rates, the mode with the lowest frequency (i.e. the slowest decay rate in imaginary time) shall give dominate contributions, while contributions from high-frequency modes are suppressed and sub-leading due to the larger decay rates. As a result, the 2nd (i.e. the higher frequency $A_{S^x,2}$) mode suffers more from noise and numerical uncertainty in both the simulations and the procedure of analytical continuation, as we convert imaginary time QMC data to real frequency. This is the main reason why the error-bar and uncertainty associated with the high-energy (amplitude) mode $A_{S^x,2}$ is much larger, in comparison with the low-energy one. This problem and numerical error can be efficiently suppressed by apply a staggered pinning field (h). As shown in the main text, the pinning field pins the direction of the order parameter to z , and thus the phase and amplitude modes now are diverted into two different correlation functions $\langle S_x S_x \rangle$ and $\langle S_z S_z \rangle$, respectively. As a result, in $\langle S_z S_z \rangle$, there is no phase mode and the amplitude mode becomes the lowest frequency mode with dominant contribution to the imaginary-time QMC data, which leads to a much sharper amplitude-mode peak in comparison with $h = 0$ case.

It is also worthwhile to point out that in the theory picture above, we ignored higher order contributions from finite-size effects in Eq. (S45). Thus, finite-size analysis and extrapolation are still needed to directly compare theory predictions and numerical experiments in the thermodynamic limit. In Fig. S4, we plot A_{S^x} at $k = (\pi, \pi/2)$ at $h = 0$, where two features (peaks) emerge in the quasi-1D limit (small g). Upon increasing the system size L , the frequency of the 2nd peak decreases. Association of the 2nd peak with the 2nd breather of the sine-Gordon model implies that its energy should reach $\sqrt{3}\Delta_0$ in the $L = \infty$ limit. Our numerical data is consistent with this prediction, even though large errors (estimated as a half-widths of the 2nd peak) make a more definite conclusion impossible.

It is worth reiterating again that our assignment of the 2nd peak to the 2nd breather is specific to $h = 0$ spectral function A_{S^x} . It relies on the spin rotational symmetry of the $L \times L$ cluster at finite temperature. As a result, spin spectral function A_{S^x} probes all spin components, much like an inelastic neutron scattering experiments with non-polarized neutrons which probe all components of the spin correlation function. Adding finite staggered h changes the situation completely. Now the 2nd breather can only be observed in the A_{S^z} spectral function, Fig. 2 (h) and (l). At the same time, solitons and anti-solitons are only present in A_{S^x} , Fig. 2 (g) and (k). Also, keep in mind that finite $h = 1/25$ changes the soliton gap Δ_0 to $\Delta_0 \sqrt{1 + b_h}$, and correspondingly the energy of the 2nd breather becomes $\sqrt{3}\Delta_0 \sqrt{1 + b_h}$.